Supplementary Information for

Scanning-exciton optical nanoscopy using a single quantum dot

Zhiyuan Wang[1,2,3†], Jiahao Han[1,2†], Xiaoqi Hou[4,5†], Jianwei Tang[1,2]*, Weixi Liu[6], Weiwang Xu[1], Zhaohua Tian[1], Hongli Chen[1,2], Jinkang Cao[1,2], Yaocheng Shi[6], Haiyan Qin[4]* and Xue-Wen Chen[1,2]*

[1] School of Physics, Wuhan National Laboratory for Optoelectronics, Institute for Quantum Science and Engineering and Hubei Key Laboratory of Gravitation and Quantum Physics, Huazhong University of Science and Technology, Wuhan 430074, China

[2] Wuhan Institute of Quantum Technology, Wuhan 430206, China

[3] College of Physics and Optoelectronics, Taiyuan University of Technology, Taiyuan 030024, China

[4] Zhejiang Key Laboratory of Excited-State Energy Conversion and Energy Storage, and Department of Chemistry, Zhejiang University, Hangzhou, 310058, China

[5] School of Chemistry and Materials Science, Hangzhou Institute for Advanced Study, University of Chinese Academy of Sciences, Hangzhou 310024, China

[6] Centre for Optical and Electromagnetic Research, State Key Laboratory of Extreme Photonics and Instrumentation, College of Optical Science and Engineering, Zhejiang University, Hangzhou 310058, China

†These authors contributed equally to this work.

*To whom correspondence should be addressed:

Jianwei Tang (jianwei_tang@hust.edu.cn);

Haiyan Qin (hattieqin@zju.edu.cn);

Xue-Wen Chen (xuewen_chen@hust.edu.cn).

Table of Contents

Supplementary Section 1 – Synthesis and characterizations of the QDs

1) A two-step procedure of QD synthesis
2) TEM characterization of the QDs
3) Spectroscopic characterization of the QDs
4) Quantum efficiency measurement of the QDs

Supplementary Section 2 – Grafting a single QD onto the apex of a silica nanotip

1) Grafting a single QD onto the apex of a silica nanotip
2) Influence of nanotip grafting on the QD's lifetime and PL intensity

Supplementary Section 3 – Experimental setups

1) Experimental setup for SEON on plasmonic nanostructures
2) Experimental setup for SEON on photonic-crystal nanobeam cavities

Supplementary Section 4 – Photostability of the QD probe

Supplementary Section 5 – Fluorescence decay rate extraction

Supplementary Section 6 – Determination of a QD's emission dipole parameters

1) QD's emission dipole model
2) Simulation and measurement of the back-focal plane image
3) Fitting the BFP patterns to determine a QD's emission dipole

Supplementary Section 7 – Characterization of the AuNS

Supplementary Section 8 – QD probe positioning and drift correction

1) Mechanical stability of the scanning probe system
2) Positioning the probe at a desired tip-substrate distance
3) Height calibration for vertical drift mitigation
4) Lateral drift correction

Supplementary Section 9 – PL intensity mapping at different QD-AuNS distances

Supplementary Section 10 – Evaluation of lateral resolution for SEON

Supplementary Section 11 – Assembly of the plasmonic trimer structure

Supplementary Section 12 – Numerical Simulations

1) Simulation of decay rate enhancement for the case of plasmonic nanostructures
2) Simulation of PL intensity enhancement for the case of plasmonic nanostructures
3) Simulation of decay rate enhancement for the case of photonic-crystal nanobeam cavity
4) Simulation of PL intensity for the case of photonic-crystal nanobeam cavity

Supplementary Section 13 – Fabrication of the photonic-crystal nanobeam cavity

Supplementary Section 14 – Reproducible SEON mapping on the photonic-crystal nanocavity

Supplementary Table 1

Supplementary Section 1 – Synthesis and characterizations of the QDs

1) A two-step procedure of QD synthesis

To achieve target wavelength and stability with minimal overall size, we epitaxially grow a thin intermediate CdSe shell and an outer ZnS shell around the CdSe core. CdSe/CdS/ZnS core/shell/shell QDs with good photochemical stability have been reported in literature[1,2]. To obtain CdSe/CdS/ZnS QDs with nearly ideal emission properties in air, we further improve the QD synthesis with a two-step procedure described as follows.

i) Synthesis and purification of zinc-blende CdSe/CdS core/shell QDs
CdO (0.5 mmol), myristic acid (1.1 mmol) and octadecene (4 mL) are loaded into a 25 mL three-neck flask. After argon bubbling for 7 min, the mixture is heated to 270 °C to obtain a colorless solution. After the temperature is reduced to 250 °C, the purified CdSe core QDs (0.06 μmol) dissolved in octadecene (0.3 mL) are injected into the mixture. 0.1 mL of sulfur dissolved in octadecene (0.1 M) is dropwise added to the reaction flask with a speed of 0.015 mL/min followed by addition of 0.1 mL oleic acid. Five minutes later, this reaction cycle is repeated until the CdS shell reaches the targeted thickness.

ii) Epitaxial growth of the ZnS outer shell
The purified CdSe/CdS QDs (0.05 μmol) in hexane, $Zn(Ac)_2 \cdot 2H_2O$ (0.5 mmol), capric acid (0.4 mmol), oleic acid (1 mmol) and 4 mL octadecene are loaded together into a 25 mL three-neck flask. The mixture is first heated to 80℃ until hexane is completely evaporated and then the temperature of the mixture is raised to 300℃. Sulfur dissolved in octadecene (0.1 M) is dropwise added into the reaction flask with a speed of 2 mL/h and 0.1 mmol of oleic acid is added to the reactor every 10 min. The reasons for doing this are to avoid inter-particle ripening and to assist in removing excess H_2S-related species which may serve as surface traps. The reaction is proceeded until the CdSe/CdS/ZnS core/shell/shell QDs with a targeted size are obtained.

2) TEM characterization of the QDs

We perform transmission electron microscopy (TEM) to characterize the size of the QDs. Supplementary Fig. 1a displays a TEM image of a batch of the zinc-blende CdSe core QDs. Supplementary Fig. 1b shows a histogram of the sizes, which indicates that the CdSe cores have a mean size of 3.0 nm with a standard deviation of 0.3 nm. Supplementary Fig. 1c displays a TEM image of a batch of zinc-blende CdSe/CdS/ZnS core/shell/shell QDs. A high-resolution TEM image of a typical dot is depicted in the inset with a scar bar of 5 nm. It reveals hexahedral structure of the QDs[3]. Size statistics (Supplementary Fig. 1d) indicates that the CdSe/CdS/ZnS core/shell/shell QDs have an average size of 6.6 nm with a standard deviation of 0.6 nm.

3) Spectroscopic characterization of the QDs

The absorption and emission spectra of the QD ensembles in solution are plotted in black and red solid traces in Supplementary Fig. 1e. The dashed trace represents the PL emission spectrum of a typical single QD on a coverslip surface. The emission spectrum has a peak around 605 nm and a full-width-of-half-maximum of 17 nm. Supplementary Fig. 1f shows the photoluminescence decay curve from a representative single QD on the coverslip, which exhibits monoexponential decay dynamics with a lifetime of 33.10 ± 0.04 ns.

4) Quantum efficiency measurement of the QDs

The absolute PL quantum efficiency of the QD ensemble is measured by using an integrating sphere (FOIS-1, Ocean Optics) coupled with a spectrometer (QE65000, Ocean Optics). The system is calibrated with a standard light source (DH-3-cal, Ocean Optics). Measurements are performed for QDs in toluene at room temperature with a 450 nm light-emitting-diode as the excitation light source. The absolute PL quantum efficiency of the QD ensemble is measured to be 96%.

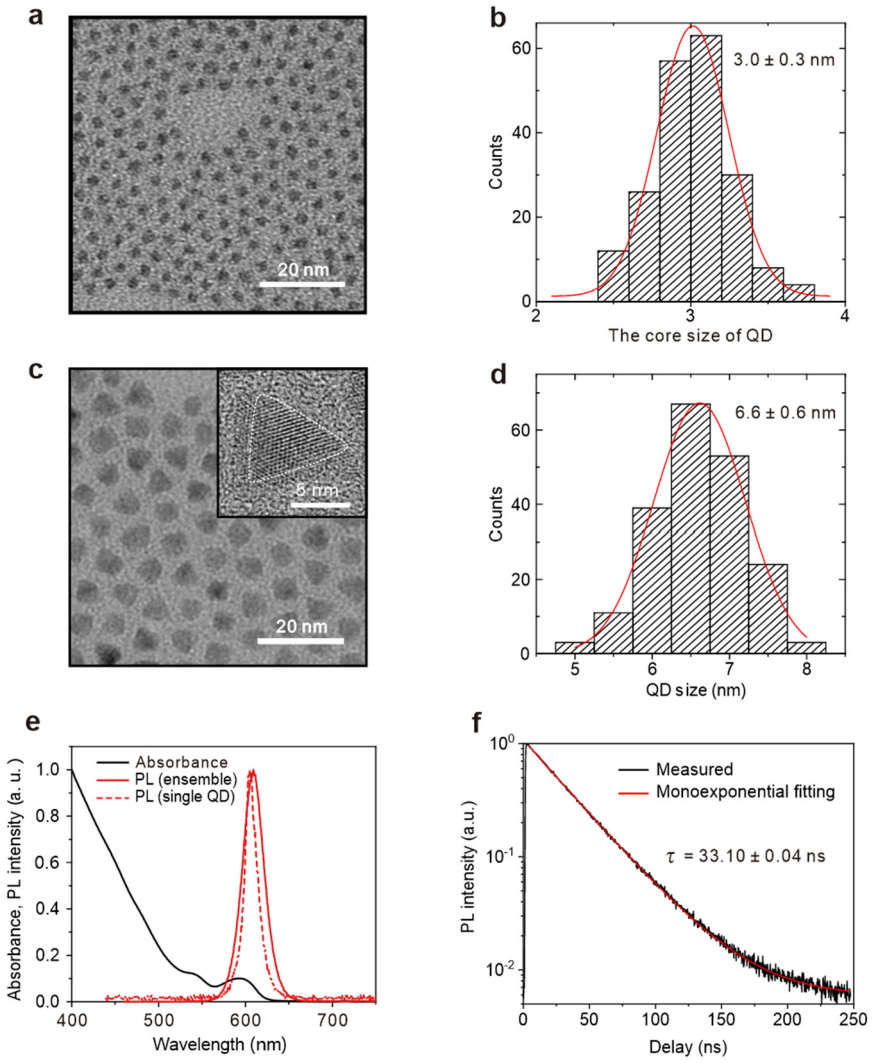

Supplementary Fig. 1 Morphology, size and spectroscopic information of the synthesized QDs. **a** TEM image of the zinc-blende CdSe core QDs. **b** Size statistics of the CdSe core QDs, obtained from TEM images. The CdSe core QDs have a mean size of 3.0 nm with a standard deviation of 0.3 nm. **c** TEM image of the zinc-blende CdSe/CdS/ZnS core/shell/shell QDs. Inset: an enlarged TEM image of a typical QD. **d** Size statistics of the CdSe/CdS/ZnS core/shell/shell QDs, obtained from TEM images. The QDs have a mean size of 6.6 nm with a standard deviation of 0.6 nm. **e** Absorbance and photoluminescence spectra of the QDs. The black and red solid lines show the absorbance and photoluminescence spectra of the ensemble QDs, respectively. The red dashed line shows the photoluminescence spectrum of a representative single QD on a coverslip. The ensemble QDs have a photoluminescence peak around 607 nm with a full-width at half-maximum of 28 nm. The single QD has a photoluminescence peak around 605 nm and a full-width at half-maximum of 17 nm. **f** Photoluminescence decay curve from a representative single QD on the coverslip, exhibiting monoexponential decay dynamics with a lifetime of 33.10 $\pm$ 0.04 ns, where the uncertainty is the fitting uncertainty (1σ).

Supplementary Section 2 – Grafting a single QD onto the apex of a silica nanotip

1) Grafting a single QD onto the apex of a silica nanotip

Initially, a silica nanotip is made by pulling a single-mode fiber (Nufern 630-HP SMF) until its break with a micropipette puller (P-2000, Sutter). The nanotip is characterized using scanning electron microscopy (SEM). Supplementary Fig. 2 presents the SEM image of the nanofiber tip, revealing that the tip apex has a diameter of approximately 40 nm.

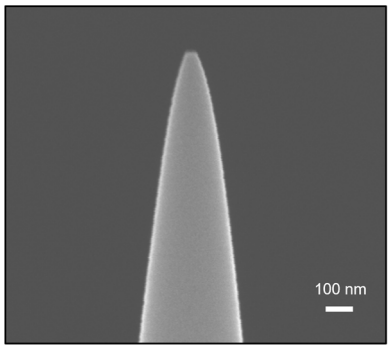

Supplementary Fig. 2 Scanning electron microscopy (SEM) image of the nanofiber tip. The SEM image reveals that the tip apex has a diameter of approximately 40 nm.

Subsequently, the base of the nanotip is glued to one arm of a tuning fork mounted onto a 3D piezoelectric nanopositioner. The tuning fork mounted on the nanopositioner is used to regulate the tip-sample distance via shear-force feedback—a standard configuration in scanning near-field optical microscopy (SNOM) for maintaining a fixed, non-contact probe height above the sample surface during scanning. In this way, the nanotip can be controllably scanned in 3D space with high precision.

The next step is to graft a single QD to the nanotip apex. The procedure is illustrated in Supplementary Fig. 3a. A sample of isolated QDs on a clean coverslip is prepared and imaged under an inverted optical microscope. A specific QD is chosen as the target, and the nanotip is positioned above it using the nanopositioner. The nanotip is then vertically lowered towards the QD, gently pressed against the QD, and subsequently lifted. This process results in the QD being attached to the tip with a high probability. Supplementary Figs. 3b and 3c display the fluorescence images captured before and after a single QD is successfully grafted onto the nanotip.

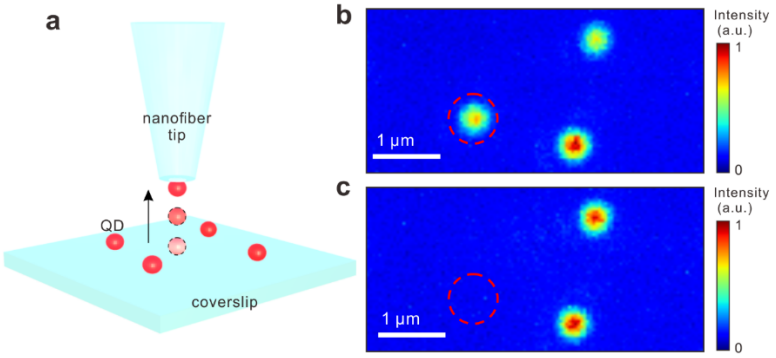

Supplementary Fig. 3 Grafting a single colloidal QD onto the tip of a nanofiber. **a** Schematics of the QD picking-up procedure. **b** Wide-field fluorescence image of single QDs on the coverslip. The QD with a red-dashed circle is the target QD to be picked up to the scanning nanotip. **c** Wide-field fluorescence image after the QD is picked up by the nanotip and retracted away from the coverslip surface.

2) Influence of nanotip grafting on the QD's lifetime and PL intensity

We measured and compared the PL intensities and lifetimes of the same QD before and after it is grafted to the apex of the silica nanotip. The results are presented in Supplementary Fig. 4. We observe that grafting the QD to the silica nanotip does not appreciably modify the QD's PL lifetime and intensity, implying that the integration process does not introduce new non-radiative decay channels or modify the absorption cross-section of the QD.

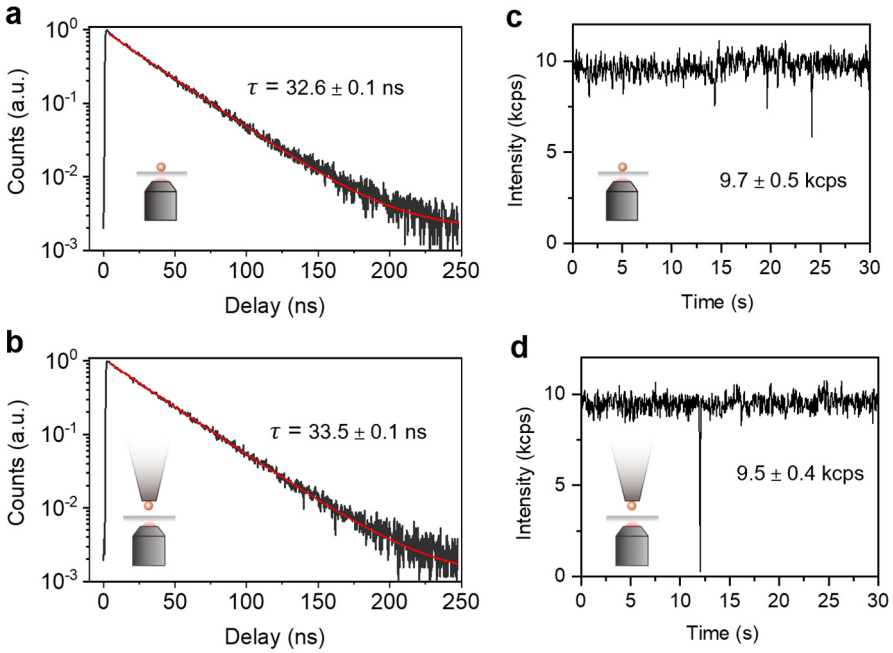

Supplementary Fig. 4 Influence of nanotip grafting on the QD's lifetime and PL intensity. **a**, **b** PL decay curve of a QD before (**a**) and after (**b**) grafting to the silica nanotip. After nanotip grafting, the PL lifetime shows a slight increase, i.e., from 32.6 ns for the QD on the glass substrate to 33.5 ns for the QD grafted on the fiber tip. **c**, **d** PL intensity time trace of the QD before (**c**) and after (**d**) grafting to the silica nanotip. After nanotip grafting, the PL intensity shows a slight decrease, i.e., from 9.7 kcps for the QD on the glass substrate to 9.5 kcps for the QD grafted on the fiber tip.

Supplementary Section 3 – Experimental setups

1) Experimental setup for SEON on plasmonic nanostructures

The experimental setup for SEON on plasmonic nanostructures is shown in Supplementary Fig. 5. We combine an inverted microscope, a tip-scanning head with a tuning fork module and atomic force microscopy (AFM) module exchangeable (NanoWizard-III, JPK), and a time-correlated single photon counting unit (TCSPC, Picoharp 300, Picoquant). A controller unit synchronizes the tip scanner, sample scanner and the TCSPC unit by sending TTL pulses as marker signals. For fluorescence intensity and decay rate measurement, a 532 nm pulsed laser (~ 100 ps, 4.03 MHz repetition rate) filtered from a white light super-continuum source (SC-Pro, YSL Photonics) launches excitation to the sample through an objective (NA = 1.4, UPlanSApo 100×, Olympus). The fluorescent photons from the QD on the tip are collected by the same objective, filtered and detected by an avalanche photodiode (APD). The APD signal and the electronic sync signal from the pulsed laser are both sent to the TCSPC unit. The APD signal is also sent to the control unit. Note that one may use any excitation wavelength that is significantly shorter than the QD's emission wavelength so that the excitation light can be filtered out (by optical filters) from PL signal. When one performs SEON with a specific excitation wavelength, the mapping of PL intensity reveals the light intensity distribution at that specific wavelength. Here we set the excitation wavelength at 532 nm for several noncritical reasons: 532 nm is one of the most commonly available wavelengths for laser light sources; 532 nm is not too far beyond the band edge of the QD so that the emission of the QD is better behaved; 532 nm is close to the plasmonic resonance of the gold nanoparticles.

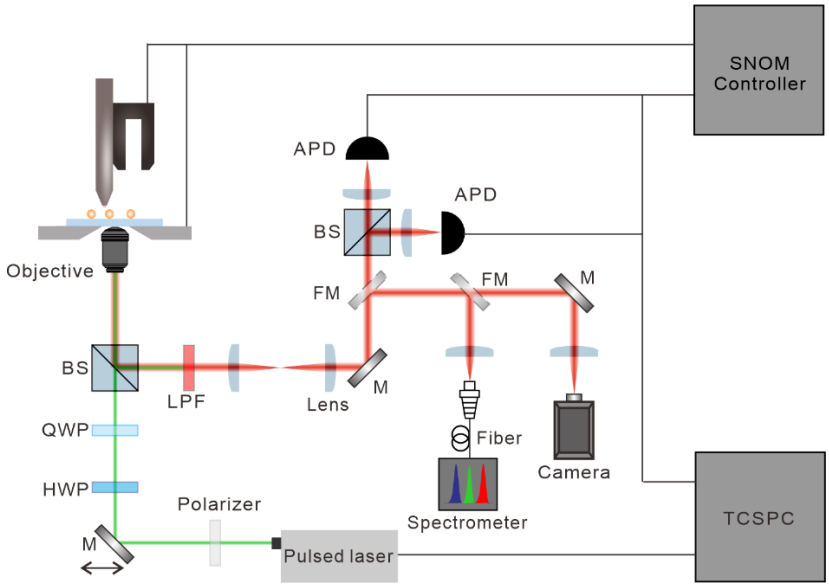

Supplementary Fig. 5 Schematic diagram of the setup for SEON experiment on plasmonic nanostructures. BS: beam splitter; LPF: long pass filter; M: mirror; FM: flip mirror; APD: avalanche photodiode; TCSPC: Time-correlated single-photon counting.

2) Experimental setup for SEON on photonic-crystal nanobeam cavities

The experimental setup for SEON on photonic-crystal nanobeam cavities, illustrated in Supplementary Fig. 6, is adapted from the configuration used for SEON on plasmonic nanostructures. In this setup, fluorescence photons generated by the QD undergo spatial separation through two distinct emission channels: a portion couples into the cavity and radiates out of the chip through a grating coupler (denoted as S_1), while the residual emission radiates directly into free space (denoted as S_2). Both the emission components S_1 and S_2 are simultaneously collected by

the objective. To enable independent detection of S_1 and S_2, a D-shaped mirror (DM) is employed in the optical path to split the field of view into two discrete detection arms. This arrangement facilitates the routing of S_1 and S_2 to APD_1 and APD_2, respectively, for time-correlated single-photon detection.

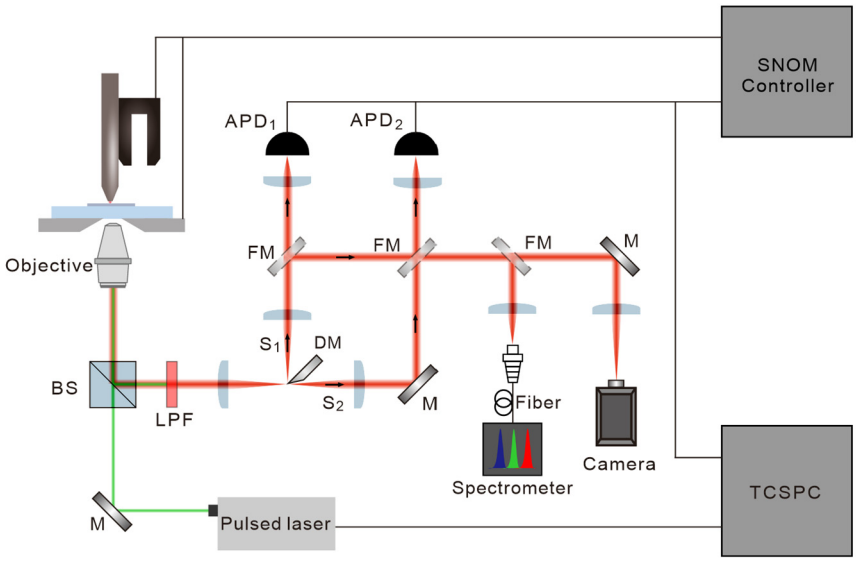

Supplementary Fig. 6 Schematic diagram of the setup for SEON experiment on photonic-crystal nanobeam cavities. BS: beam splitter; LPF: long pass filter; M: mirror; DM: D-shaped mirror; FM: flip mirror; APD: avalanche photodiode; TCSPC: Time-correlated single-photon counting.

Supplementary Section 4 – Photostability of the QD probe

Supplementary Fig. 7 presents the time trace of the scanning QD probe's PL intensity for over three hours. The QD on the scanning tip continuously fluoresces for over three hours without degradation, demonstrating the probe's excellent photostability.

Two types of intensity fluctuation are observed in the time trace: (i) transient transitions to dark states, and (ii) slow fluctuations in bright-state PL intensity. Neither compromises mapping fidelity.

(i) The transient transitions to dark states in the time trace stem from QD fluorescence blinking—a well-documented intrinsic property of single quantum emitters. Quantitative analysis shows these dark states account for < 2% of the total PL emission duration.

To mitigate their influence on imaging fidelity, dark-state segments were identified and excluded from PL intensity and decay rate mapping analysis. Additionally, all mappings are constructed by averaging multiple independent scanning frames. Critically, QD blinking is random and transient: the dark-state events occur unpredictably at different time points and do not correlate with specific spatial positions. In other words, a dark-state event that affects one small spatial region in a single frame will not repeat at the same spatial region in other frames. This randomness ensures that no fixed spatial region is "consistently missed" (i.e., excluded due to dark states) across all frames. As a result, the final averaged image is free of voids caused by blinking.

(ii) The slow drifts in bright-state PL intensity originate from QD height drifts induced by environmental perturbations (e.g., air currents, temperature fluctuations). The height drifts alter the QD's distance from the substrate, leading to variations in fluorescence collection efficiency.

Critically, the slow drifts observed here in the PL intensity time trace do not compromise the fidelity of the mappings, as in mapping experiments we implement a dedicated tip height calibration routine to ensure consistent tip height throughout the entire imaging process (Supplementary Section 8.3).

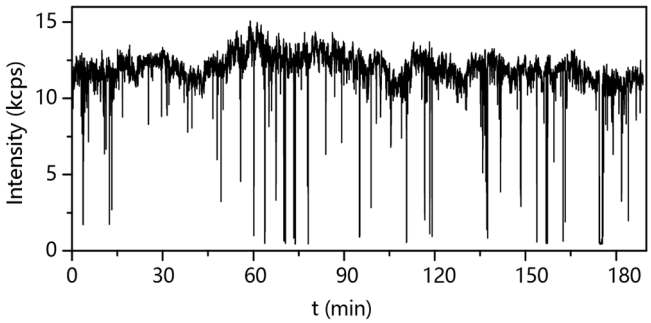

Supplementary Fig. 7 A representative PL intensity time trace of the QD probe. The QD on the scanning tip continuously fluoresces for over three hours without degradation.

Supplementary Section 5 – Fluorescence decay rate extraction

Our single QD probe possesses high quantum yield and almost perfect mono-exponential PL decay dynamics, which allow us to get the correct fluorescence decay rate from a small number of photon counts. For mono-exponential decay dynamics, the PL decay curve can be expressed as $p(t) = A\mathrm{e}^{-\gamma t}$, where t is the time delay between the photon arrival time and the excitation pulse, and γ is the decay rate. Thus the decay rate can be obtained via $\gamma = \int A\mathrm{e}^{-\gamma t}\mathrm{d}t / \int tA\mathrm{e}^{-\gamma t}\mathrm{d}t$.

Note that all PL decay rates extracted in our experiments fall well within the response bandwidth of our TCSPC system, thus eliminating the need for deconvolution, as detailed below. The experimentally measured PL decay curve is the convolution of the true decay curve with the system's instrument response function (IRF). When the true decay rate (γ_{true}) approaches or exceeds the IRF's characteristic decay rate (γ_{IRF}), this convolution artificially prolongs the measured decay time, resulting in underestimated $\gamma_{\mathrm{measure}}$. In contrast, for $\gamma_{\mathrm{true}} \ll \gamma_{\mathrm{IRF}}$, the convolution effect is negligible, and $\gamma_{\mathrm{measure}} \approx \gamma_{\mathrm{true}}$. Supplementary Fig. 8a presents the IRF of our TCSPC system. And the relation between $\gamma_{\mathrm{measure}}$ and γ_{true} derived from this IRF is shown by the solid curve in Supplementary Fig. 8b. For $\gamma_{\mathrm{true}} \leqslant (1\ \mathrm{ns})^{-1}$, this curve aligns with the dashed $y = x$ line. Crucially, all decay rates measured in our experiments fall within this linear regime, and thus $\gamma_{\mathrm{measure}}$ can be directly taken as γ_{true}, without the need for deconvolution.

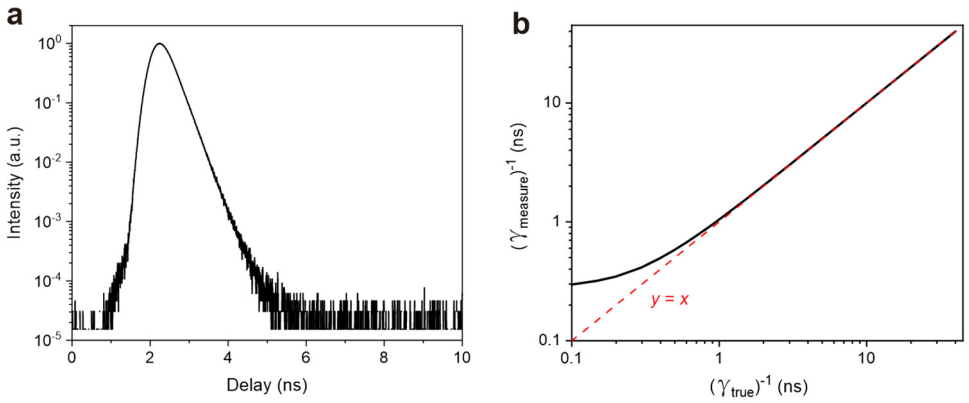

Supplementary Fig. 8 Influence of instrument response function (IRF) on decay rate measurement. **a** Instrument response function (IRF) of the time-correlated single-photon counting (TCSPC) system used in this study. **b** The relation between the measured decay rate ($\gamma_{\mathrm{measure}}$) and the true decay rate (γ_{true}), derived from the IRF presented in panel **a**. The red dashed line represents the ideal $y = x$ relation, corresponding to an infinitely fast temporal response of the TCSPC system.

Supplementary Section 6 – Determination of a QD's emission dipole parameters

1) QD's emission dipole model

The commonly-used 2D degenerate dipole model[4] is inconsistent with our measurements. Therefore, on top of the 2D model, we introduce an extra dipole $\mathbf{u}_3$ perpendicular to the 2D dipole plane spanned by two orthogonal dipoles $\mathbf{u}_1$ and $\mathbf{u}_2$ with the same magnitude. These dipoles are incoherent to each other. As illustrated in Supplementary Fig. 9a, the QD's emission dipole can be described by the orientation of $\mathbf{u}_3$ in terms of (θ, φ) and the amplitude ratio $R = |\mathbf{u}_3/\mathbf{u}_1|$. For $R \rightarrow 0$ the model reduces to the usual 2D dipole while for $R \gg 1$, the model reduces to a 1D dipole.

2) Simulation and measurement of the back-focal plane image

The emission pattern of single-QD fluorescence can be characterized by imaging the radiation pattern at the back-focal plane (BFP) of the objective. Numerical simulation of the emission pattern of a radiating electric dipole is carried out by first applying the 3D finite-difference time-domain (FDTD) method[5] to obtain the near field and then performing a near-to-far field transformation[6] to obtain the far field. The computation volume is set to be 15μm×15μm×1μm to ensure the convergence of the emission pattern obtained via a near-to-far field transformation. Electric fields at the far field are calculated and stored for three orthogonal dipole orientations and then can be used to generate the field for an arbitrarily oriented dipole through superposition. For the emission dipole described by $(\mathbf{u}_1, \mathbf{u}_2, \mathbf{u}_3)$, we first apply the superposition approach for each dipole $\mathbf{u}_i$ and then incoherently add the intensity to obtain the overall BFP pattern. To compare with the experimental observation, we consider the actual numerical aperture (NA) values as well as the effect of the objective lens which collimates the spherical rays.

Experimental measurement of the BFP pattern is performed as follows. The fluorescence is collected by the oil immersion objective (NA=1.4, UPlanSApo 100×, Olympus) and the BFP of the objective is imaged to a SCMOS camera (C13440-20CU, Hamamatsu) with a 0.2× magnification. To record the BFP images, the camera works in sequence acquisition mode and the exposure time for every frame is set to 10 seconds. About 20 consecutive frames are superimposed to obtain a BFP pattern. The final BFP pattern is obtained by further subtracting the background BFP pattern, which corresponds to the pattern in the same configuration but without the QD on the nanotip. Supplementary Fig. 9b shows the BFP pattern of a QD probe.

3) Fitting the BFP patterns to determine a QD's emission dipole

The emission dipole of a QD, i.e., parameters (R, θ, φ), can be determined by matching the measured BFP image with the calculated one. To quantify how good the fitting is, we employ the cosine similarity $\mu_{\cos}$ between the measured and simulated BFP patterns, which reads[7]

$$\mu_{\cos} \equiv \frac{\mathbf{A}\cdot\mathbf{B}}{\|\mathbf{A}\|\|\mathbf{B}\|} = \frac{\sum_{i=1}^{n} A_i B_i}{\sqrt{\sum_{i=1}^{n} A_i^2}\sqrt{\sum_{i=1}^{n} B_i^2}}, \tag{S1}$$

where **A** and **B** are the two vectors representing the measured and simulated BFP patterns, respectively. We perform a direct 3D scan in the parameter space of (R, θ, φ) and find the globally best fit at the optimal parameter set. The value of $\mu_{\cos}$ as a function of the parameters (R, θ, φ) is displayed in a 3D iso-surface plot in Supplementary Fig. 9c. A global maximum is observed at (R = 3.1, θ = 89°, φ = 145°). The cosine similarity distribution in the (θ, φ) plane for R = 3.1 is re-plotted in Supplementary Fig. 9d. The BFP pattern for the best fit is plotted in Supplementary Fig. 9e and indeed resembles the measured image (Supplementary Fig. 9b).

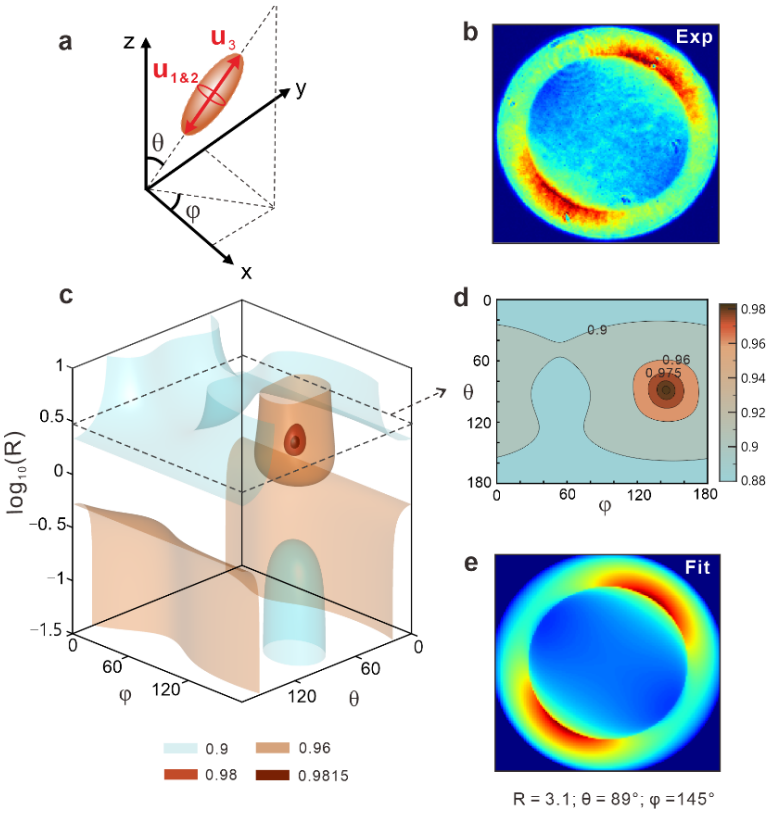

Supplementary Fig. 9 Determination of the dipole structure and orientation of a single QD by fitting a measured back-focal plane (BFP) pattern. **a** Illustration of a single QD's emission dipole model. **b** Measured BFP pattern of a QD probe. **c** A 3D iso-surface plot of cosine similarity $\mu_{\cos}$ between the simulated and measured BFP patterns as a function of the scanned parameters θ, φ and R. There is a clear global maximum located at $\theta = 89^{\circ}$, $\varphi = 145^{\circ}$, and $R = 3.1$. **d** Cosine similarity distribution as a function of (θ, φ) for $R = 3.1$ (marked by the dashed square in **c**). **e** Simulated BFP pattern at the global maximum of the similarity, which resembles the measured BFP pattern.

Supplementary Section 7 – Characterization of the AuNS

Atomic force microscopy (AFM) is employed to characterize the dimensional characteristics of the AuNS. Supplementary Fig. 10a presents an AFM topographic image of the AuNS used in Fig. 2 of the main text. The corresponding cross-sectional profile extracted along the central cutline yields a measured diameter of 76.4 nm. The dark-field scattering spectrum of the AuNS is shown in Supplementary Fig. 10b, which exhibits a localized surface plasmon resonance at ~ 540 nm.

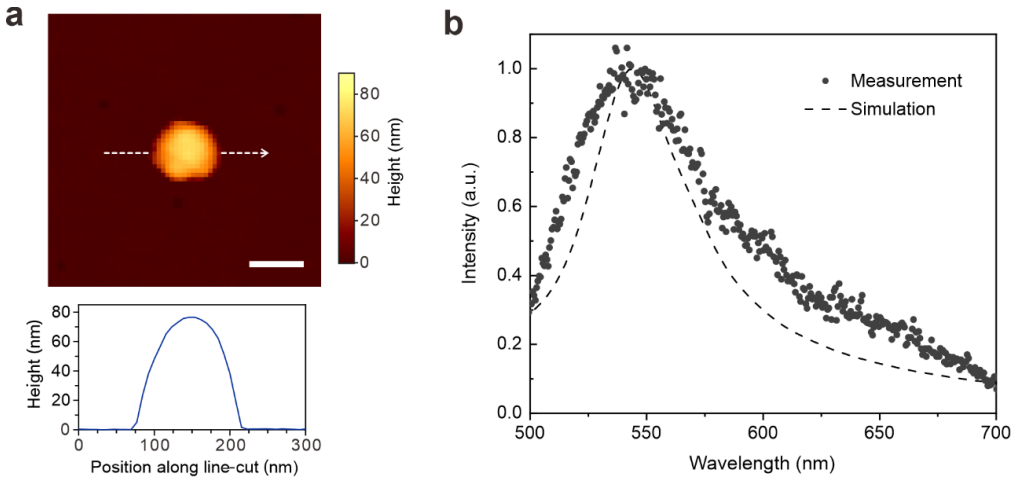

Supplementary Fig. 10 Morphological and spectroscopic characterizations of the AuNS used in Fig. 2 of the main text. **a** AFM topographic image of the AuNS. The corresponding cross-sectional profile along the dashed cutline is displayed in the lower panel. Scale bar, 100 nm. **b** Dark-field scattering spectrum of the AuNS, showing a localized surface plasmon resonance at ~540 nm.

Supplementary Section 8 – QD probe positioning and drift correction

1) Mechanical stability of the scanning probe system

Supplementary Fig. 11 shows the real-time height fluctuations of the scanning tip after it reaches the set point and is parked at a fixed height with the feedback electronics on. The feedback electronics exhibits high sensitivity in maintaining the tip-substrate distance constant. If the substrate vibrates, the tip will follow this motion to preserve a constant distance. In our system, we observe that the tip exhibits a vertical drift rate of approximately 1 nm per 8 minutes. Such excellent stability allows us to have a fixed tip-substrate distance for several scanning frames when the feedback electronics is tuned off.

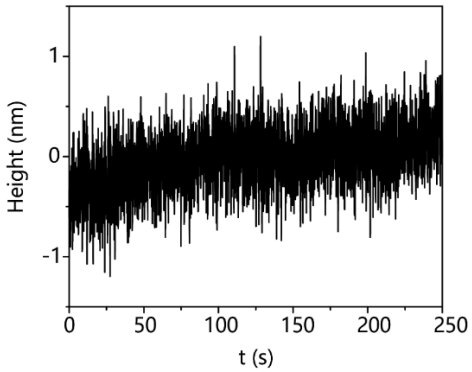

Supplementary Fig. 11 Real-time height fluctuations of the scanning tip with the feedback turned on. These fluctuations are recorded as length changes of the piezoelectric nanopositioner.

2) Positioning the probe at a desired tip-substrate distance

To place the tip at a desired tip-substrate distance, we first tune the set point of the feedback to move the tip. Once the tip is at the desired height, a small feedback gain (0.1 ~ 0.3 Hz) can counterbalance the slow rise trend and quickly stabilize the tip. Then one can further decrease the feedback gain and perform SEON measurement at this specific tip-substrate distance.

3) Height calibration for vertical drift mitigation

High-quality PL intensity and decay rate enhancement mappings require averaging multiple scanning frames, which may result in prolonged total imaging time. To mitigate cumulative height drift over extended imaging, we implement a height calibration routine: every N frames (where N is chosen such that the total duration of N frames is ~ 3 minutes—an interval where drift remains insignificant), we bring the probe into gentle contact with the substrate surface and reposition it to the target height. This calibration routine ensures consistent tip height throughout the entire imaging process.

Notably, the QD probe maintains excellent stability against repeated substrate contact during calibration. For instance, the mappings in Figs. 5d and 5e were obtained via averaging 126 scanning frames, which requires ~ 30 times of substrate contact; throughout this process, the QD probe maintained consistent emission properties.

4) Lateral drift correction

Lateral drifts are corrected during post-processing using the following strategy: After acquiring scanning data, we first average every consecutive N frames (consistent with the interval for vertical calibration) to generate N-frame-averaged sub-maps; We then calculate the lateral drift vector between each subsequent N-frame-averaged sub-map and the first N-frame-averaged sub-map (used as the reference) via cross-correlation; All sub-maps are aligned based on the derived drift vectors to eliminate positional deviations.

Supplementary Section 9 – PL intensity mapping at different QD-AuNS distances

Supplementary Fig. 12 presents the PL intensity enhancement mapping under three types of in-plane excitation polarizations at different vertical QD-AuNS distances (d = 2.6, 5.6, 8.6, and 11.6 nm). Intensity profiles similar to those presented in Fig. 2 are observed for these distances.

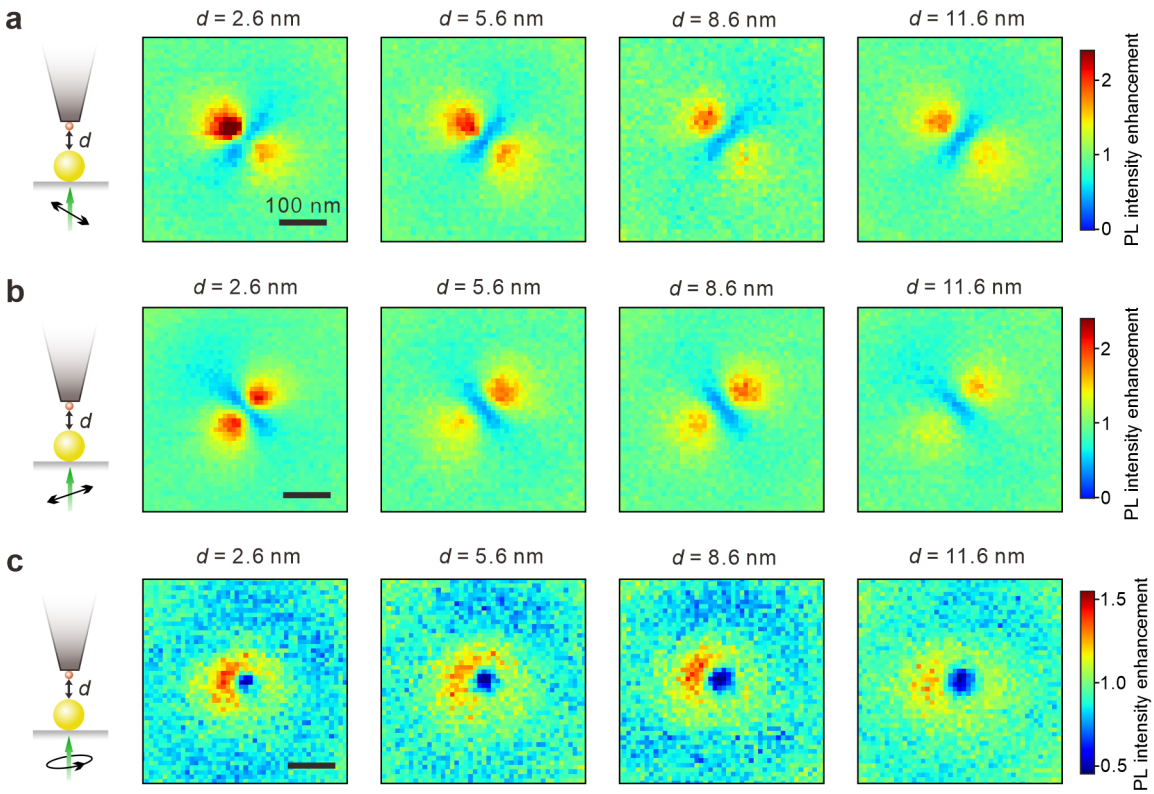

Supplementary Fig. 12 PL intensity enhancement mapping under three types of in-plane excitation polarizations at different vertical QD-AuNS distances. PL intensity enhancement mappings obtained via SEON on a gold nanosphere (AuNS) under three types of in-plane excitation polarizations, i.e., two orthogonal in-plane linear polarizations (**a**, **b**) and a circular polarization (**c**). The vertical QD-AuNS distance d is indicated at each PL intensity enhancement mapping. The QD probe's dipole parameters (R, θ, φ) = (2.8, 77°, 52°). Scale bars, 100 nm.

Supplementary Section 10 – Evaluation of lateral resolution for SEON

To quantitatively determine the lateral resolution of SEON, we employ a convolution fitting method, which is widely recognized in scanning probe microscopy for resolving lateral resolution when the probe's finite size broadens the measured near-field profile.

Principle

The experimentally measured lateral profile of the AuNS's near-field is the convolution of two components: (1) the "true" lateral near-field profile of the AuNS (obtained via numerical simulations); (2) the lateral response function of the QD probe (approximated as a Gaussian function with FWHM = X, where X is the lateral resolution to be extracted). By fitting the experimental profile to the convolved simulated profile, we can accurately extract X.

Fitting procedure

We first acquire the experimental lateral decay rate profile by extracting the cross-sectional data along a cutline through the hotspot center of the experimental decay rate mapping. We then convolve the simulated profile with Gaussian functions of varying FWHMs and compare each convolved profile with the experimental data. The optimal fit is determined by minimizing the root-mean-square error (RMSE) between the convolved profile and the experimental data.

As shown in Supplementary Fig. 13, the best fit to the experimental decay rate profile (black dots) is achieved when the Gaussian FWHM is 4 nm (red curve). Thus, the lateral resolution of SEON is quantified as 4 nm.

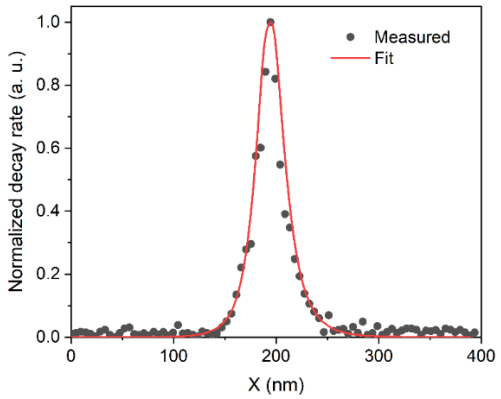

Supplementary Fig. 13 Convolution fitting for lateral resolution evaluation. Black dots represent the cross-sectional data extracted along a cutline through the hotspot center of the decay rate profile experimentally acquired 2 nm above the AuNS (top panel of Fig. 3c of the main text). The red curve denotes the optimal fit, which is the convolution of the finite-difference time-domain (FDTD)-simulated "true" decay rate profile of the AuNS with a Gaussian function (full-width at half-maximum (FWHM) = 4 nm). The FWHM of this Gaussian function defines the lateral resolution of SEON.

Supplementary Section 11 – Assembly of the plasmonic trimer structure

Initially, colloidal AuNSs (from BBI Solutions) are transferred onto a coverslip via drop-casting. Subsequently, the coverslip is rinsed with deionized water and cleaned via plasma cleaning to remove residual ligands from the surface of the AuNSs. AFM topography measurements are performed for AuNSs on the substrate to select AuNSs with desired sizes. Then the selected AuNSs are pushed to the specified locations with the AFM tip. Tapping mode is used for both AFM imaging and nanomanipulation[8,9]. The plasmonic trimer structure shown in Fig. 4 is made through this approach.

Supplementary Section 12 – Numerical Simulations

1) Simulation of decay rate enhancement for the case of plasmonic nanostructures

The radiative spontaneous emission rate of an excited atom, or the radiative exciton decay rate, is not an intrinsic property of the atom or exciton, but is rather dependent on its immediate electromagnetic environment defined by LDOS. Specifically, the radiative spontaneous emission rate γ_{rad} of an emitter at position $\mathbf{r}_0$ with transition frequency ω_0 in a structured photonic environment can be expressed as[10,11] $\gamma_{\mathrm{rad}} = \frac{\pi\omega_0}{3\hbar\varepsilon_0}|\mathbf{p}|^2\rho_{\mathrm{p}}(\mathbf{r}_0,\omega_0)$, where $\rho_{\mathrm{p}}(\mathbf{r}_0,\omega_0)$ is the LDOS related to the photonic structure via the Green's tensor $\overleftrightarrow{\mathbf{G}}$ as $\rho_{\mathrm{p}}(r_0,\omega_0) = \frac{6\omega_0}{\pi c^2}\mathrm{Im}\left[\mathbf{u}\cdot\overleftrightarrow{\mathbf{G}}(\mathbf{r}_0,\mathbf{r}_0,\omega_0)\cdot\mathbf{u}\right]$. Here Im[…] denotes the imaginary part, **u** is the unit vector of the transition (emission) dipole moment $\mathbf{p}$, and $\hbar$, ε_0 and c are the reduced Planck's constant, electric permittivity in vacuum and speed of light in vacuum, respectively. Thus LDOS can be modified by the photonic structures and depend on the dipole orientation. The radiative decay rate enhancement factor $\gamma_{\mathrm{rad}}/\gamma_{\mathrm{rad}}^{\mathrm{o}}$ (where $\gamma_{\mathrm{rad}}^{\mathrm{o}}$ is the radiative decay rate for the reference case) can be obtained by comparing the LDOS with a reference case. Numerically it is the ratio of the radiated powers from an electric dipole $\gamma_{\mathrm{rad}}/\gamma_{\mathrm{rad}}^{\mathrm{o}} = P/P^{\mathrm{o}}$, where P and P^{o} stand for the total radiation power of the electric dipole coupled to the photonic structures and for the reference case, respectively. The total radiation power of the emitter P can be evaluated by integrating the Poynting vector over a closed surface, which incorporates the dipole but excludes any absorptive media. Numerical simulations of the electromagnetic responses of the structure for a radiating dipole and a planewave excitation are performed using the finite element method with a commercial software (COMSOL Multiphysics).

To compare the radiative decay rate enhancement factor $\gamma_{\mathrm{rad}}/\gamma_{\mathrm{rad}}^{\mathrm{o}}$ with the experimentally measurement decay rate enhancement factor $\gamma/\gamma^{\mathrm{o}}$, one should generally take into account the intrinsic nonradiative decay rate of the emitter $\gamma_{\mathrm{nrad}}^{\mathrm{o}}$ (which doesn't change with the photonic environment) via $\gamma = \gamma_{\mathrm{rad}} + \gamma_{\mathrm{nrad}}^{\mathrm{o}}$ and $\gamma^{\mathrm{o}} = \gamma_{\mathrm{rad}}^{\mathrm{o}} + \gamma_{\mathrm{nrad}}^{\mathrm{o}}$. The intrinsic nonradiative decay rate $\gamma_{\mathrm{nrad}}^{\mathrm{o}}$ is related to the intrinsic quantum yield η^{o} of the emitter as $\eta^{\mathrm{o}} = \gamma_{\mathrm{rad}}^{\mathrm{o}}/(\gamma_{\mathrm{rad}}^{\mathrm{o}} + \gamma_{\mathrm{nrad}}^{\mathrm{o}})$. In our study, since the absolute PL quantum efficiency of the QD ensemble is measured to be 96%, the quantum yield of a single QD at its "on" state should be close to 100% considering the fluorescence intermittency (blinking between "on" state and "off" state). Then we could reasonably assume an intrinsic quantum yield of 100% for the numerical simulations, i.e, we could neglect the nonradiative decay. Thus, we have $\gamma/\gamma^{\mathrm{o}} = \gamma_{\mathrm{rad}}/\gamma_{\mathrm{rad}}^{\mathrm{o}} = P/P^{\mathrm{o}}$.

2) Simulation of PL intensity enhancement for the case of plasmonic nanostructures

The PL intensity enhancement factor f_{PL} is calculated via $f_{\mathrm{PL}} = f_{\mathrm{ex}}\cdot f_{\eta}\cdot f_{\mathrm{c}}$, where f_{ex} is the excitation enhancement factor, f_{η} is the quantum yield enhancement factor and f_{c} is collection efficiency enhancement factor. The calculations of f_{ex}, f_{η} and f_{c} are described below.

i) Excitation enhancement factor f_{ex}

We launch a plane source in normal incidence or oblique incidence with respect to the interface from the glass substrate side to excite the structure and the QD on the nanotip. For transverse magnetic polarized excitation in total internal reflection an incidence angle of 50° is assumed. The excitation enhancement factor f_{ex} is defined as the

ratio of the excitation intensity with the photonic structures to the excitation intensity without the photonic structures. A simulated map of excitation enhancement is obtained by scanning the position of the nanotip as in the experiments.

ii) Quantum yield enhancement factor f_η

The quantum yield enhancement factor $f_\eta = \eta/\eta^o$, where $\eta^o = \gamma_{rad}^o/(\gamma_{rad}^o + \gamma_{nrad}^o)$ is the intrinsic quantum yield of the emitter and $\eta = \gamma_{rad}/(\gamma_{rad} + \gamma_{nrad}^o)$ is the quantum yield of the emitter coupled to the photonic structures. Note that here the defined quantum yield doesn't include the loss due to the photonic structures.

For quantum emitters with non-unity quantum yield (i.e., $\eta^o < 1$), the enhancement of the radiative decay rate would lead to a quantum yield $\eta > \eta^o$. While for quantum emitters with unity intrinsic quantum yield (i.e., $\eta^o = 1$), we have $\gamma_{nrad}^o = 0$ and thus $\eta = \eta^o = 1$, i.e., the quantum yield enhancement factor $f_\eta = 1$. In this study, the quantum yield of the QDs at the "on" state could be assumed 100%, so we simply put $f_\eta = 1$.

iii) Collection efficiency enhancement factor f_c

The collection efficiency enhancement factor f_c is the ratio of the collection efficiency with the photonic structures to the collection efficiency without the photonic structures. The collection efficiency is defined as the ratio of the power collected by the objective to the power released by the emitter. Note that here the power released by the emitter includes the power dissipated in the photonic structures. So in the collection enhancement factor f_c the modification of the radiation efficiency by the gold nanoparticles has been taken into account. Accordingly, in the numerical simulation, the collection efficiency is defined as the ratio of the dipole power collected by the objective to the total dipole power. The total dipole power is calculated by integrating the Poynting vector over a closed surface enclosing the dipole source. The objective with a NA of 1.4 can collect almost all the dipole power radiated to the substrate side, so the dipole power collected by the objective is calculated by integrating the Poynting vector over a plane just below the substrate surface that is large enough to collect the power radiated to the substrate side.

Supplementary Fig. 14a and 14b respectively show the simulated map of excitation enhancement (f_{ex}) and collection efficiency enhancement (f_c) for the plasmonic trimer in Fig. 4. Since $f_\eta = 1$, the simulated map of PL intensity enhancement (f_{PL}) is then obtained via $f_{PL} = f_{ex} \cdot f_c$, as shown in Supplementary Fig. 14c.

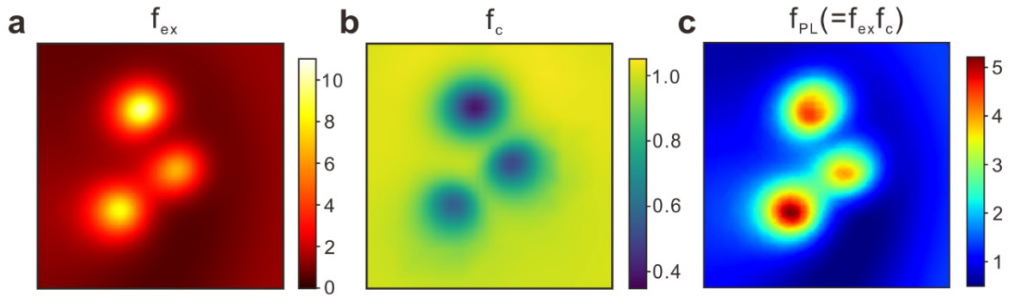

Supplementary Fig. 14 Simulation of enhancements of excitation, collection efficiency and fluorescence intensity for the sample structure (the plasmonic trimer) studied in Fig. 4 of the main text. Simulated maps of excitation enhancement (**a**), collection efficiency enhancement (**b**) and PL intensity enhancement (**c**). The PL intensity enhancement factor f_{PL} is the product of the excitation enhancement factor f_{ex} and the collection enhancement factor f_c.

3) Simulation of decay rate enhancement for the case of photonic-crystal nanobeam cavity

Unlike plasmonic nanostructures, since the linewidth of the photonic-crystal nanocavity is narrower than that of the quantum dot, it is necessary to calculate the decay rate enhancement at each frequency point within the spectral range of the quantum dot. So in this case, the decay rate enhancement of the quantum dot is calculated via $\gamma_{\mathrm{QD}}/\gamma_{\mathrm{QD}}^{\mathrm{o}} = \int f_{\mathrm{p}}(\omega)\, S_{\mathrm{QD}}^{\mathrm{o}}(\omega)\, \mathrm{d}\omega$, where $S_{\mathrm{QD}}^{\mathrm{o}}(\omega)$ is the normalized fluorescence spectrum of the QD in vacuum, $f_{\mathrm{p}}(\omega)$ denotes the radiative decay rate enhancement as a function of frequency. Numerically, the enhancement of the radiative decay rate can be quantified as the ratio between the total radiation powers emitted by an electric dipole in the presence and absence of the nanobeam cavity $f_{\mathrm{p}}(\omega) = \gamma_{\mathrm{rad}}(\omega)/\gamma_{\mathrm{rad}}^{\mathrm{o}}(\omega) = P(\omega)/P^{o}(\omega)$. To efficiently acquire the radiation power spectrum, the simulation is performed using the FDTD (finite-different time-domain) method with a commercial software (Lumerical FDTD).

4) Simulation of PL intensity for the case of photonic-crystal nanobeam cavity

The PL intensity $I \propto f_{\mathrm{ex}} \cdot f_{\eta} \cdot \beta$, where f_{ex} is the excitation enhancement factor, f_{η} is the quantum yield enhancement factor and β is the coupling efficiency. The calculations of f_{ex}, f_{η} and β are described below.

i) Excitation enhancement factor f_{ex}

In the experiment, the excitation light is vertically focused onto the QD through a 0.7-NA objective lens from the substrate side. In the simulation, the excitation light is modeled as a Gaussian beam focused by a 0.7-NA thin lens. By scanning the position of the nanobeam, the excitation intensity at the quantum dot locations can be calculated. Since the excitation intensity changes only slightly during the movement of the photonic-crystal nanocavity, f_{ex} can be approximated as a constant.

ii) Quantum yield enhancement factor f_{η}

In our study, the quantum yield of the QD at the "on" state could be assumed 100%, so the quantum yield enhancement factor $f_{\eta} = 1$.

iii) Coupling efficiency β

The coupling efficiency β is the ratio of the power coupling to the photonic-crystal nanocavity mode to the total radiation power from the QD. Due to the finite linewidth of the QD, the coupling efficiency is calculated via $\beta = \int \beta_{\omega}(\omega)\, S_{\mathrm{QD}}(\omega)\, \mathrm{d}\omega$, where $S_{\mathrm{QD}}(\omega)$ is the normalized spectrum of the QD, $\beta_{\omega}(\omega)$ represents the frequency-dependent coupling efficiency. Note that here the spectrum of the QD is modified by the cavity. Therefore, $S_{\mathrm{QD}}(\omega) = f_{\mathrm{pn}}(\omega)\, S_{\mathrm{QD}}^{\mathrm{o}}(\omega)$, where $f_{\mathrm{pn}}(\omega)$ denotes the normalized radiative decay rate enhancement by the photonic-crystal nanocavity, and $S_{\mathrm{QD}}^{\mathrm{o}}(\omega)$ is the normalized spectrum of the QD in vacuum.

The frequency-dependent coupling efficiency $\beta_{\omega}(\omega)$ is calculated as follows. The fluorescence coupled into the photonic-crystal nanocavity will further couple to the TE_0 mode of the waveguide and eventually be collected. The power coupled into the TE_0 mode is $P_{\mathrm{m}}(\omega) = \frac{1}{4}(\int E \times H_{\mathrm{m}}^{*}\, \mathrm{d}S + \int E_{\mathrm{m}}^{*} \times H\, \mathrm{d}S)^2 / \int E_{\mathrm{m}} \times H_{\mathrm{m}}^{*}\, \mathrm{d}S$, where E and H are the electric and magnetic field distributions at the waveguide cross-section located near the edge of the photonic-crystal nanocavity, and E_{m} and H_{m} are the electric and magnetic field distributions of the TE_0 mode of the waveguide. The total dipole power $P(\omega)$ is calculated by integrating the Poynting vector over a closed surface enclosing the dipole source. The frequency-dependent coupling efficiency can then be calculated via $\beta_{\omega}(\omega) = P_{\mathrm{m}}(\omega)/P(\omega)$.

Supplementary Section 13 – Fabrication of the photonic-crystal nanobeam cavity

The suspended photonic-crystal nanobeam cavity is fabricated on a 500-μm-thick JGS2 quartz glass substrate. Initially, a 130 nm-thick silicon nitride (Si_3N_4) film is deposited on the substrate via low-pressure chemical vapor deposition (LPCVD) and subsequently annealed at 1100°C for one hour. A 300-nm-thick ZEP520A photoresist layer is subsequently spin-coated onto the surface of the Si_3N_4 film. The photoresist mask patterns for the photonic-crystal nanobeam cavity and the input/output gratings are then defined using electron beam lithography (EBL). The patterns are subsequently transferred into the Si_3N_4 layer by inductively coupled plasma (ICP) dry etching, selectively removing unmasked Si_3N_4 regions. Post-etching, the residual photoresist is completely removed using piranha solution (H_2SO_4:H_2O_2 = 3:1). To suspend the photonic-crystal nanobeam cavity structure, the device undergoes isotropic etching in 85°C KOH solution (1:1 mass ratio with deionized water) for 1 hour. This isotropic etching process creates an etching depth of approximately 1 μm, effectively suspending the photonic-crystal nanobeam cavity structure while preserving its mechanical integrity.

Supplementary Section 14 – Reproducible SEON mapping on the photonic-crystal nanocavity

The dual-parameter mapping on the waveguide-interfaced photonic-crystal nanocavity (presented in Fig. 5) is reproducible, as shown in Supplementary Fig. 15. Specifically, Supplementary Fig. 15a and 15b display the PL intensity and PL decay rate enhancement mappings, respectively, obtained using another QD probe.

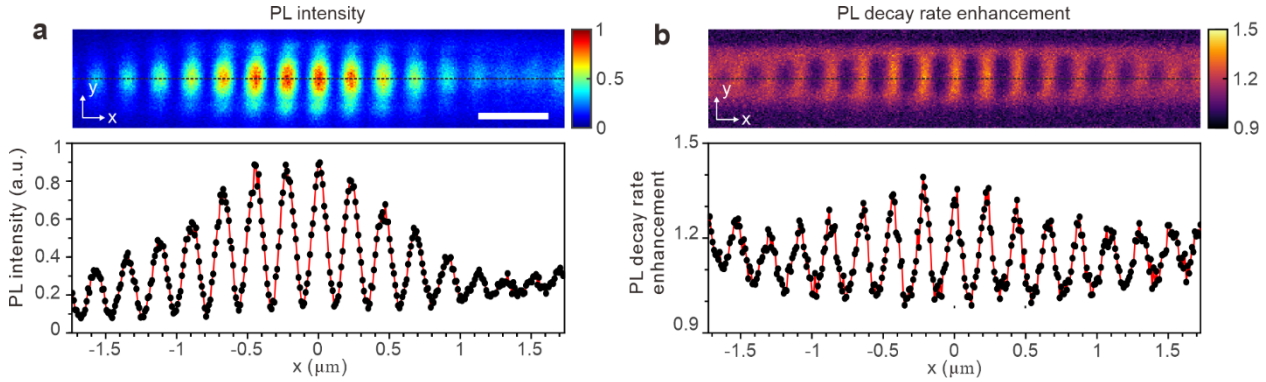

Supplementary Fig. 15 SEON on the waveguide-interfaced photonic-crystal nanocavity using another QD probe. **a** PL intensity mapping for the nanocavity. Cross-sectional plot along the dashed line is shown below the mapping. Scale bar, 500 nm. **b** PL decay rate enhancement mapping for the nanocavity. Cross-sectional plot along the dashed line is shown below the mapping. The QD probe's dipole parameters (R, θ, φ) = (2.4, 83°, 77°).

Supplementary Table 1 Scanning parameters for the mappings in this study

	number of frames averaged	**scanning time per frame (s)**	**total dwell time per pixel (ms)**
Fig. 2a,d	8	11	31
Fig. 2b,e	11	11	43
Fig. 2c,f	9	11	35
Fig. 3b,c (d = 2 nm)	3	22	6
Fig. 3b,c (d = 4 nm)	3	22	6
Fig. 3b,c (d = 6 nm)	2	22	4
Fig. 3b,c (d = 8 nm)	2	22	4
Fig. 4b,c	9	32	18
Fig. 5d,e	126	39	201
Supplementary Fig. 12a (d = 2.6 nm)	8	11	31
Supplementary Fig. 12a (d = 5.6 nm)	9	11	35
Supplementary Fig. 12a (d = 8.6 nm)	7	11	27
Supplementary Fig. 12a (d = 11.6 nm)	10	11	39
Supplementary Fig. 12b (d = 2.6 nm)	11	11	43
Supplementary Fig. 12b (d = 5.6 nm)	7	11	27
Supplementary Fig. 12b (d = 8.6 nm)	9	11	35
Supplementary Fig. 12b (d = 11.6 nm)	8	11	31
Supplementary Fig. 12c (d = 2.6 nm)	9	11	35
Supplementary Fig. 12c (d = 5.6 nm)	11	11	43
Supplementary Fig. 12c (d = 8.6 nm)	7	11	27
Supplementary Fig. 12c (d = 11.6 nm)	11	11	43
Supplementary Fig. 15	78	39	124

References

1. Talapin, D. V., Mekis, I., Gotzinger, S., Kornowski, A., Benson, O. & Weller, H. CdSe/CdS/ZnS and CdSe/ZnSe/ZnS core-shell-shell nanocrystals. *Journal of Physical Chemistry B* **108**, 18826-18831 (2004).
2. Cao, Z. Y., Shu, Y. F., Qin, H. Y., Su, B. & Peng, X. G. Quantum Dots with Highly Efficient, Stable, and Multicolor Electrochemiluminescence. *ACS Central Science* **6**, 1129-1137 (2020).
3. Zhou, J., Zhu, M., Meng, R., Qin, H. & Peng, X. Ideal CdSe/CdS Core/Shell Nanocrystals Enabled by Entropic Ligands and Their Core Size-, Shell Thickness-, and Ligand-Dependent Photoluminescence Properties. *Journal of the American Chemical Society* **139**, 16556-16567 (2017).
4. Empedocles, S. A., Neuhauser, R. & Bawendi, M. G. Three-dimensional orientation measurements of symmetric single chromophores using polarization microscopy. *Nature* **399**, 126-130 (1999).
5. Taflove, A. & Hagness, S. C. *Computational electrodynamics: the finite-difference time-domain method*. (Artech house, 2005).
6. Zhang, P., Ren, P. L. & Chen, X. W. On the emission pattern of nanoscopic emitters in planar anisotropic matrix and nanoantenna structures. *Nanoscale* **11**, 11195-11201 (2019).
7. O'toole, A. J., Deffenbacher, K. A., Valentin, D. & Abdi, H. Structural aspects of face recognition and the other-race effect. *Memory & Cognition* **22**, 208-224 (1994).
8. Tang, J. W., Xia, J., Fang, M. D., Bao, F. L., Cao, G. J., Shen, J. Q., Evans, J. & He, S. L. Selective far-field addressing of coupled quantum dots in a plasmonic nanocavity. *Nature Communications* **9**, 1705 (2018).
9. Xia, J., Tang, J., Bao, F., Sun, Y., Fang, M., Cao, G., Evans, J. & He, S. Turning a hot spot into a cold spot: polarization-controlled Fano-shaped local-field responses probed by a quantum dot. *Light: Science & Applications* **9**, 166 (2020).
10. Joulain, K., Carminati, R., Mulet, J. P. & Greffet, J. J. Definition and measurement of the local density of electromagnetic states close to an interface. *Physical Review B* **68**, 245405 (2003).
11. Novotny, L. & Hecht, B. *Principles of Nano-Optics- 2nd Edition*. (Cambridge University Press, New York, 2012).